


Cite this: *RSC Adv.*, 2022, 12, 16688

# A probe-free electrochemical immunosensor for methyl jasmonate based on a Cu-MOF-carboxylated graphene oxide platform†

Gengqi Xing,<sup>†ab</sup> Cheng Wang,<sup>†a</sup> Ke Liu,<sup>a</sup> Bin Luo,<sup>a</sup> Peichen Hou,<sup>a</sup> Xiaodong Wang,<sup>a</sup> Hongtu Dong,<sup>a</sup> Jianshu Wang<sup>\*b</sup> and Aixue Li<sup>ib\*ab</sup>

Methyl jasmonate (MeJA) is an important phytohormone which can regulate plant growth and stress tolerance. It is very necessary to develop sensitive and accurate detection methods for MeJA. In this work, a probe-free electrochemical immunosensor for MeJA detection was developed based on a Cu-MOF-carboxylated graphene oxide (COOH-GO) platform. The Cu<sup>2+</sup> in the Cu-MOFs was used to provide redox signals, which avoids the application of an external redox probe in the electrolyte solutions as conventional immunosensors. COOH-GO was used to improve the structural stability and provide more sites for binding MeJA antibodies. The linear range of the MeJA immunosensor is from 10 pM to 100 μM, which can cover the whole concentration range of MeJA in most plants. And its detection limit is very low (0.35 pM), and it can detect very low concentrations of MeJA. This immunosensor is simple, low cost, and does not need redox probe solutions for measurements. It shows remarkable potential for on-site application in precision agriculture.

Received 18th October 2021

Accepted 16th May 2022

DOI: 10.1039/d1ra07683c

rsc.li/rsc-advances

## 1. Introduction

Methyl jasmonate (MeJA, Fig. 1A) is the methylated derivative of jasmonic acid (JA), which is widely found in higher plants.<sup>1</sup> As an important phytohormone of plants, MeJA participates in the regulation of a wide range of physiological processes, such as seed germination, flowering, fruit ripening, and leaf senescence.<sup>2,3</sup> MeJA also participates in intra-plant and inter-plant communication, and plays a particularly important role in enhancing plant defense response to biotic and abiotic stresses.<sup>3</sup> Moreover, MeJA also shows good application and development potential in the storage and preservation of fruits,<sup>4</sup> treatment of cancer,<sup>5</sup> *etc.* Therefore, it is very necessary to develop sensitive and accurate detection methods for MeJA. Recently, electrochemical immunosensors have attracted considerable attention because of their advantage of good selectivity and sensitivity, portability, low cost, and ease of integration. They have been used to achieve quantitative detection of several plant hormones, including indole-3-acetic acid (IAA),<sup>6,7</sup> abscisic acid (ABA),<sup>8</sup> and gibberellin (GA).<sup>9</sup>

However, as far as we know, the electrochemical immunosensor for MeJA has rarely been reported.

Label-free electrochemical immunosensors have attracted great interest due to their no complex labeling process. This kind of sensor usually requires redox probes in the electrolyte solutions to generate amperometric signal that is proportional to the formed antigen/antibody complexes.<sup>10</sup> However, one of the main disadvantages of this method is time consuming and labor intensive.<sup>11</sup> Recently, redox probe-free platforms have been developed for immunosensors.<sup>12,13</sup> In this kind of sensor, the redox probes are modified on the sensor surface to provide redox signals for electrochemical readings, without the need of external redox probe in the electrolyte solutions as conventional immunosensors,<sup>14</sup> which is an important advancement towards real point-of-care testings. Redox-active moieties, such as ferrocene (Fc) and its derivatives, can be used as electrochemical signal probes in this kind of immunosensors. Our group have developed a probe-free electrochemical immunosensor for MeJA based on Fc functionalized-carboxylated graphene-multi-walled carbon nanotube nanocomposites.<sup>15</sup> However, to develop new probes or new methods for immobilizing these probes is still needed.

Metal-organic frameworks (MOFs) are promising materials constructed from metal ion nodes linked together by organic linkers. It has rich metal active sites, high porosity, and chemical tenability, *etc.*<sup>16,17</sup> Based on these unique features, MOFs present a huge potential for electrochemical application. It's also worth noting that the metal ions in some MOFs have redox activity, so they can be used as electrical signal probes in the

<sup>a</sup>Intelligent Equipment Research Center, Beijing Academy of Agriculture and Forestry Sciences, Beijing 100097, China. E-mail: aixueli\_2021@163.com; liax@nercita.org.cn

<sup>b</sup>College of Landscape and Ecological Engineering, Hebei University of Engineering, Handan 056038, China. E-mail: wangjianshu135@163.com

† Electronic supplementary information (ESI) available. See <https://doi.org/10.1039/d1ra07683c>

‡ These authors contributed equally to this work.



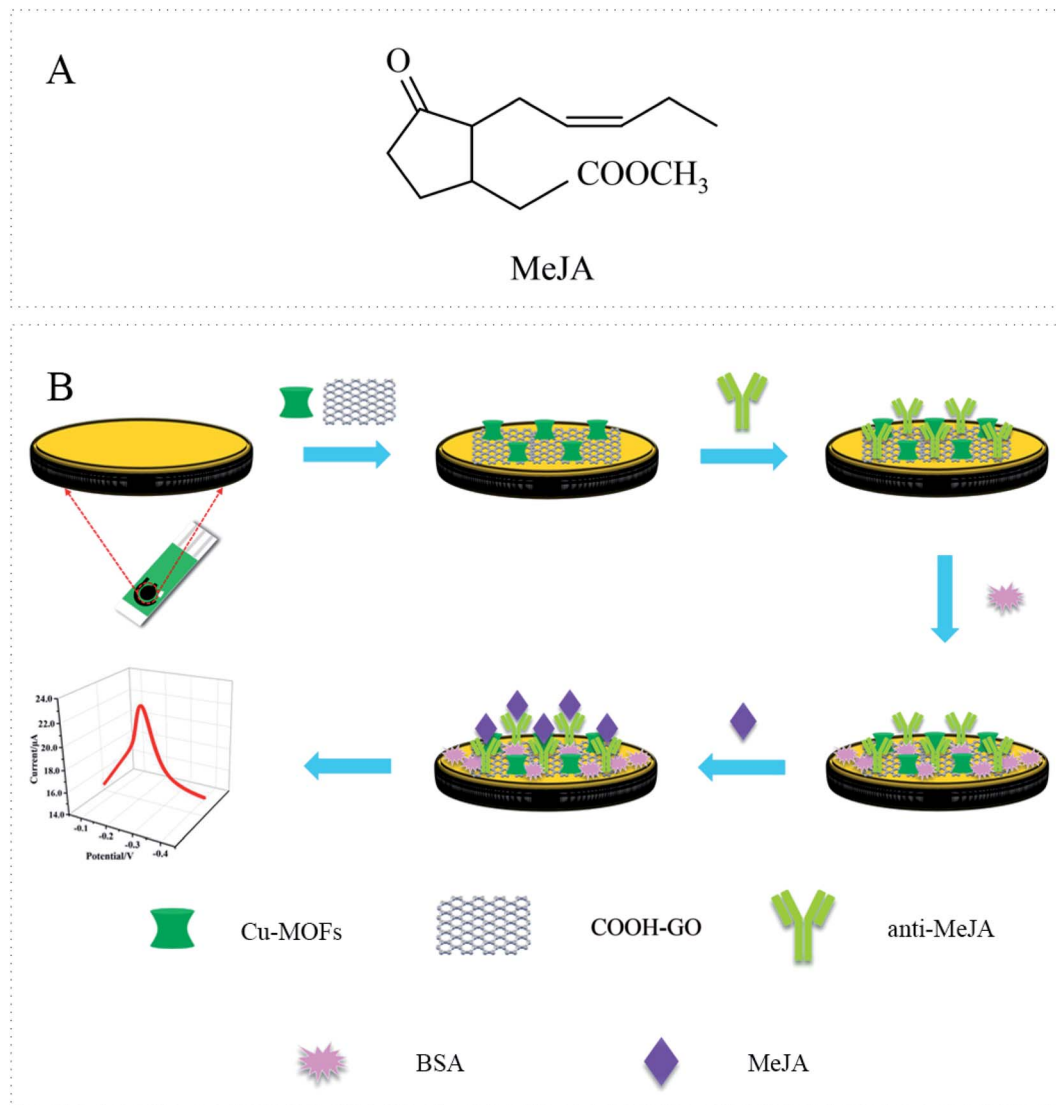


Fig. 1 (A) Molecular formula of MeJA. (B) Schematic illustration of the construction process of the electrochemical immunosensor of MeJA.

construction of electrochemical sensors in recent years. For example, Song *et al.* developed a ratiometric electrochemical glucose biosensor based on GOD/AuNPs/Cu-BTC MOFs/macroporous carbon integrated electrode,<sup>18</sup> in which the redox peak of Cu-BTC MOFs was used as a reference signal. In addition to acting as the redox probe in the electrochemical sensors, MOFs also have high specific surface area and good adsorption properties, which can be used to load antibody. However, no immunosensors has been reported for MeJA detection based on MOFs as the redox probes.

The application of single phase MOFs in electrochemical sensor is limited because of its instability in aqueous solution, easily collapsed structure and weak conductivity.<sup>19</sup> The introduction of highly conductive carbon-based nanomaterials, such as graphene (GR), carbon nanotubes (CNT), carbon black *etc.* has been proved to be an effective strategy to improve the stability and conductivity of MOFs. For example, Zhang *et al.* reported a hybrid sensor based on copper-based metal organic

frameworks (Cu-MOFs)/macroporous carbon (MPC).<sup>20</sup> Rani *et al.* developed a new type of hydrazine sensor, which modified Zn-MOFs@rGO (reduced graphene oxide) composite to the gold electrode surface.<sup>21</sup> These studies shows that the composite material composed of carbon materials and MOFs not only has good electrocatalytic performance for analytes, but also has structural stability in water medium, which helps to improve the detection performance of the sensor.

In this work, we developed a probe free immunosensor for MeJA based on Cu-MOFs-carboxylated graphene oxide platform. Carboxylated graphene oxide (COOH-GO) was used to form nanocomposite with Cu-MOFs due to its large specific surface area, high conductivity, good biocompatibility and so on.<sup>22,23</sup> The formed Cu-MOFs-COOH-GO nanocomposites not only have good redox activity and stability, but also provide more sites for antibodies immobilization. Screen-printed electrodes (SPEs) are more practical and low-cost, so our sensor was fabricated on it. The fabricated immunosensor shows high



sensitivity and wide detection range. Our strategy can be easily used to develop immunosensors for other potential analytes.

## 2. Materials and methods

### 2.1. Reagents

Polyvinylpyrrolidone (PVP), *N,N*-dimethylformamide (DMF), 2-amino terephthalic acid ( $\text{NH}_2\text{-BDC}$ ), 1-(3-dimethylaminopropyl)-3-ethylcarbodiimide hydrochloride (EDC), *N*-hydroxysuccinimide (NHS), Nafion solution (5 wt%) and Bovine Serum Albumin (BSA) were purchased from Sigma-Aldrich reagent Co., Ltd (St. Louis, MO, USA). Carboxylated graphene oxide (COOH-GO) was obtained from XFNANO materials Tech Co., Ltd (Nanjing, China). Methyl jasmonate standards ( $\text{C}_{13}\text{H}_{20}\text{O}_3$ , 98%) were purchased from Aladdin Chemistry Co., Ltd (Shanghai, China). Phosphate buffer solution (PBS, 0.01 M, pH 7.4) was obtained from Solarbio Tech Co., Ltd (Beijing, China). Copper nitrate trihydrate ( $\text{Cu}(\text{NO}_3)_2 \cdot 3\text{H}_2\text{O}$ ), potassium ferricyanide ( $\text{K}_3[\text{Fe}(\text{CN})_6]$ ), potassium ferrocyanide ( $\text{K}_4[\text{Fe}(\text{CN})_6]$ ), potassium chloride (KCl) and sodium acetate trihydrate (NaAc) were obtained from Sinopharm Chemical Reagent Co., Ltd (Beijing, China). MeJA monoclonal antibody (anti-MeJA) was obtained from China Agricultural University. The remaining reagents were of analytical grade. Solutions were prepared using double distilled water throughout the experiment.

### 2.2. Apparatus

A FESEM system (ZEISS, SEM 500, Germany) equipped with an EDS microprobe was used for investigating the morphologies of Cu-MOFs and the different modified SPE electrodes. Glassy carbon sheets with diameter of 5 mm were applied for the SEM and EDS-mapping characterization. X-ray diffraction (XRD) patterns were achieved through a Smart Lab X-ray diffractometer (Rigaku, Japan) using Cu-K ( $\alpha$ ) radiation. FTIR spectra were collected with a VERTEX 70v FTIR spectrometer in the range of 400–4000  $\text{cm}^{-1}$  (Bruker, Germany). All electrochemical immunoassays were performed on CHI760E electrochemical workstation (Shanghai Chenhua Instrument Co., China). Commercial screen printed electrodes (SPEs) were purchased from Ningbo Mxense Bio-Tech Co., Ltd. The SPE has a three-electrode system consisting of carbon-based working electrode and counter electrode, and Ag/AgCl reference electrode. The diameter of the working electrode is 2.5 mm.

### 2.3. Synthesis of Cu-MOFs

Cu-MOFs was synthesized based on previous literature<sup>24</sup> with a minor modification. First, 4 ml of ethanol and 4 ml of DMF were mixed, and then 0.2 g PVP was added to the solution. Next, 23.34 mg copper nitrate trihydrate and 5.43 mg  $\text{NH}_2\text{-BDC}$  were dissolved in 4 ml DMF and mixed to the previous solution with ultrasonication for 15 min. Then the solution was poured into a Teflon-lined stainless steel autoclave and heated at 100 °C for 5 h. After adding 20 ml DMF, the reaction was continued at 100 °C for 8 h. Subsequently, the reaction mixture was cooled at room temperature and centrifuged for 3 min (10 000 rpm), and

the supernatant was removed. Finally, Cu-MOFs was obtained by drying in the drying cabinet.

### 2.4. Preparation of Cu-MOFs–COOH-GO nanocomposite

The Cu-MOFs–COOH-GO nanocomposite was obtained by mixing a certain amount of COOH-GO solution with Cu-MOFs and Nafion solution (0.5 wt%), then the mixture was added equal volume mixture of 20 mM EDC and 50 mM NHS (prepared in 0.037 M pH 5.0 acetate buffer). Then the mixed solution was ultrasounded for 1 h. The concentrations of Cu-MOFs (0.5; 0.75; 1; 1.25 and 1.5  $\text{mg ml}^{-1}$ ) and COOH-GO (0.5; 1; 1.5; 2 and 2.5  $\text{mg ml}^{-1}$ ) were optimized. COOH-GO control and Cu-MOFs control were also prepared with the similar process.

### 2.5. Construction of electrochemical immunosensor

Fig. 1B shows the construction process of the immunosensor. Before the modification, the SPE was activated in PBS buffer at 1.7 V potential for 180 s. 4  $\mu\text{l}$  of Cu-MOFs–COOH-GO nanocomposite solution was added to the electrode surface by drop casting. Then, 4  $\mu\text{l}$  of anti-MeJA solution was dropped onto the electrode surface and incubated at room temperature (24 °C) for 1 h. The concentration of anti-MeJA was also optimized. In order to block the non-specific adsorption sites, 2  $\mu\text{l}$  of 1 wt% BSA solution was dropped on the electrode and incubated at room temperature for 30 min. To remove unfixed parts, the electrode was washed carefully with PBS buffer between each step of immunosensor construction.

### 2.6. Measurement procedure

The as-prepared immunosensor was incubated with different concentrations of MeJA solution (0, 10 pM, 100 pM, 1 nM, 10 nM, 100 nM, 1  $\mu\text{M}$ , 10  $\mu\text{M}$ , 100  $\mu\text{M}$ ) for 1 hour at room temperature (24 °C). After the reaction was completed, the sensor was washed with PBS buffer to remove the unbounded materials. Differential pulse voltammetry (DPV) scan was performed in 0.01 M pH 7.4 PBS buffer under pulse amplitude of 50 mV, pulse period of 0.2 s, and pulse width of 50 ms.

### 2.7. Grape samples preparation

The grapes were purchased from local supermarket. The samples were ground with liquid nitrogen. 0.5 g of the ground powder was put into 80% ice methanol. After extraction by overnight in the refrigerator, the samples were centrifuged at 12 000 rpm for 20 minutes. A certain amount of supernatant was taken, and the recovery experiments were performed by adding MeJA standard solution to the samples.

## 3. Results and discussion

### 3.1. Characterization of immunosensors

Fig. 2(a–e) shows the characterization results of Cu-MOFs morphology and immunosensor construction process by scanning electron microscopy (SEM). The morphology of Cu-MOFs is shown in Fig. 2a. The size of the synthesized Cu-MOFs is about 2–3  $\mu\text{m}$ . They presented regular single-leaf hyperboloid



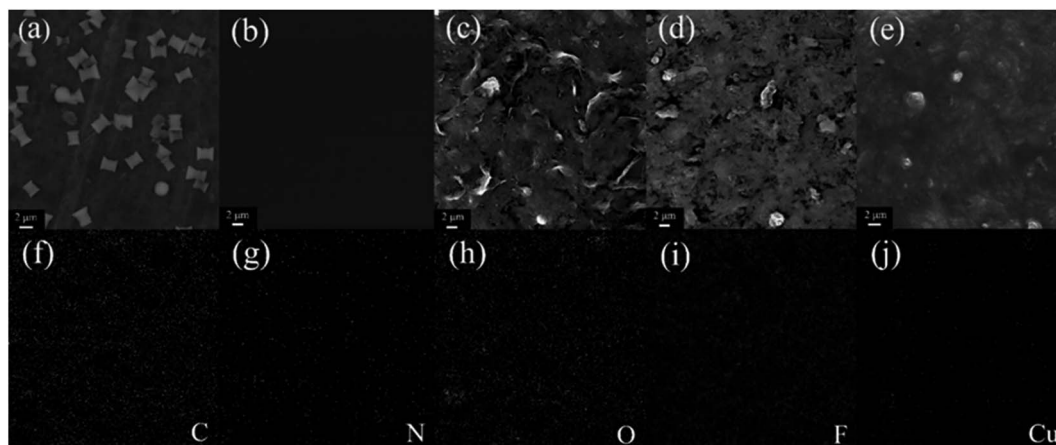


Fig. 2 SEM images of Cu-MOFs (a), bare SPE (b), Cu-MOFs-COOH-GO/SPE (c), anti-MeJA/Cu-MOFs-COOH-GO/SPE (d), BSA/anti-MeJA/Cu-MOFs-COOH-GO/SPE (e). EDS mappings of BSA/anti-MeJA/Cu-MOFs-COOH-GO/SPE (f–j).

structure which composed of single-layer nanosheets with a large surface area. The SEM image of bare SPE is shown in Fig. 2b. Its surface is smooth and clean without any impurities. When Cu-MOFs-COOH-GO nanocomposite was modified on the electrode surface, a film structure was formed on the electrode surface, and the particle structure of Cu-MOFs and the lamellar structure of COOH-GO were immersed in it (Fig. 2c). When the antibodies were modified on the electrode surface, the film became rough and the lamellar structure of COOH-GO was no longer visible which indicated that the antibody molecule had been successfully modified on the electrode surface (Fig. 2d). After adding BSA, as shown in Fig. 2e, the membrane structure became denser and rougher. Fig. 2(f–j) showed the EDS mapping analysis results of BSA/Ab/Cu-MOFs-COOH-GO/SPE, and the signals of C, O, N, F, and Cu elements were obtained. The existence of C is mainly attributed to the C element in the glassy carbon sheet, COOH-GO and Cu-MOF. The existence of O is mainly attributed to the O element in the glassy carbon sheet and COOH-GO. The presence of N is mainly attributed to the protein molecules (MeJA antibody and BSA) and the amino-functionalized Cu-MOF. Because Nafion contains F elements, it leads to the appearance of F elements. Cu ions in Cu-MOFs account for the appearance of Cu elements. Combined the result of EDS with SEM, it is proved that the electrode had been modified successfully.

The XRD characterization of COOH-GO, Cu-MOF and Cu-MOF-COOH-GO is shown in Fig. S1A.† A diffraction of  $11.5^\circ$  of  $2\theta$  is characteristic for the (001) layer of carboxyl GO.<sup>25,26</sup> As for the Cu-MOF, the diffraction peaks that appeared under  $2\theta \approx 12.1^\circ$ ,  $14.3^\circ$ ,  $17.6^\circ$ , and  $24.8^\circ$  can be attributed to the (222), (400), (440), and (444) crystal planes of Cu-MOF.<sup>27,28</sup> No peaks for Cu<sub>2</sub>O can be observed, which indicated the high purity of the Cu-MOF. As for the nanocomposite of Cu-MOF-GO, the MOF peaks are still remained, suggesting the presence of GO don't disrupted the crystallinity of Cu-MOF.<sup>29</sup> At the same time, the disappearance of d001 peak related to the destruction of the regular stacks of COOH-GO sheets.<sup>25</sup>

FTIR spectrum of the Cu-MOF, COOH-GO and their hybrids is shown in Fig. S1B.† The FTIR spectrum of COOH-GO showed a strong and broad absorption band at  $3400\text{ cm}^{-1}$  which attributed to the O–H stretching vibration.<sup>30</sup> In addition, C=O stretching vibrations at  $\approx 1700\text{ cm}^{-1}$  and C–O stretching vibrations at  $\approx 1300\text{ cm}^{-1}$  also appeared in the spectrum of COOH-GO.<sup>31</sup> As for the Cu-MOF, the peaks from 3452 and  $3351\text{ cm}^{-1}$  attributed to the formation of hydrogen bonding between the hydrogen of the amine group and oxygen of the carboxylic acid. The peaks for MOFs structure at  $1641\text{ cm}^{-1}$  can be attributed to C=C stretch.<sup>32</sup> The peak at  $1620\text{ cm}^{-1}$  owned to C=O stretching of the deprotonated tricarboxylic acid, and the bands at  $1500\text{--}1200\text{ cm}^{-1}$  are corresponding to the C–O stretching.<sup>33</sup> Vibrations of aromatic structure for the C–H bending is appeared at the region of the  $900\text{--}600\text{ cm}^{-1}$ .<sup>34</sup> The characteristic vibration for Cu–O stretching is observed at  $460\text{ cm}^{-1}$ , in which the oxygen atom was coordinated to Cu center.<sup>35</sup> The FTIR spectra of the Cu-MOF-COOH-GO shows similarities as that of Cu-MOF. The presence of IR peaks of Cu-MOF in the Cu-MOF-COOH-GO as well as their shift illustrates the successful formation of nanocomposite.<sup>36</sup>

### 3.2. Feasibilities of the fabricated immunosensor for detecting MeJA

Fig. 3A shows the DPV responses of the bare SPE, COOH-GO/SPE, Cu-MOFs/SPE and Cu-MOFs-COOH-GO/SPE in 0.01 M PBS (pH 7.4). The bare SPE (curve a) and COOH-GO/SPE (curve b) did not show any oxidation peaks in the potential range of  $-0.7\text{--}0.5\text{ V}$ . However, a distinctive oxidation peak at about  $-0.12\text{ V}$  can be observed for the DPV images of Cu-MOFs/SPE (curve c) and Cu-MOFs-COOH-GO/SPE (curve d), which was ascribed to the oxidation of Cu<sup>2+</sup> in Cu-MOFs. The oxidation peak current for the Cu-MOFs-COOH-GO/SPE is higher than that of Cu-MOFs/SPE, which might be related to the excellent characteristics of COOH-GO, such as large surface area, catalytic performance, *etc.* Therefore, Cu-MOFs-COOH-GO nanocomposites were selected for subsequent experiments.



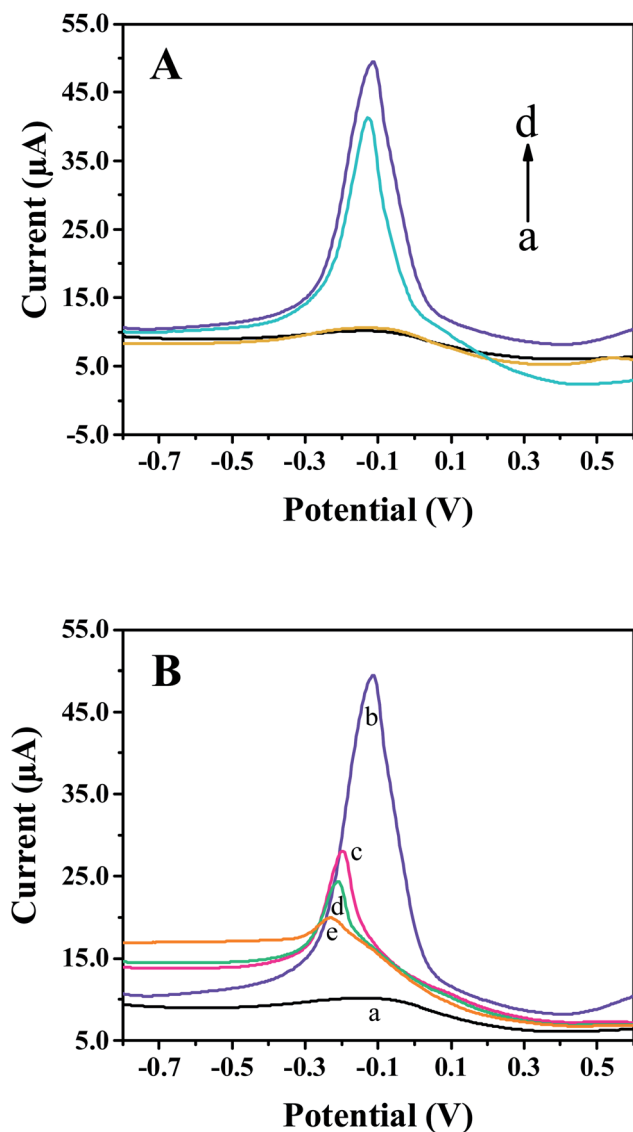


Fig. 3 (A) DPV curves of bare SPE (a), COOH-GO/SPE (b), Cu-MOFs/SPE (c), Cu-MOFs-COOH-GO/SPE (d) in 0.01 M PBS (pH 7.4). (B) DPV curves of bare SPE (a), Cu-MOFs-COOH-GO/SPE (b), anti-MeJA/Cu-MOFs-COOH-GO/SPE (c), BSA/anti-MeJA/Cu-MOFs-COOH-GO/SPE (d), and MeJA/BSA/anti-MeJA/Cu-MOFs-COOH-GO/SPE (e) in 0.01 M PBS (pH 7.4).

After modifying the electrode with Cu-MOFs-COOH-GO nanocomposites (Fig. 3B, curve b), the obvious oxidation peak of Cu-MOFs can be observed. When the electrode surface was coated with monoclonal MeJA antibody (Fig. 3B, curve c) and BSA (Fig. 3B, curve d), the oxidation peak current of Cu-MOFs decreased significantly because the non-conductive properties of antibody and proteins. The oxidation peak current of Cu-MOFs decreased further when the sensing interface was reacted with MeJA (Fig. 3B, curve e), because of the steric hindrance effect produced by the specific binding of anti-MeJA and MeJA. The difference of oxidation peak current before and after adding MeJA ( $\Delta I = I_{\text{BSA}} - I_{\text{MeJA}}$ ) can be used to detect MeJA. The DPV results confirmed that the sensor

construction process was successful and its application for detecting MeJA is feasible.

Cyclic voltammetry (CV) was used to analyze the assembly process of the immunosensor in 5 mM  $[\text{Fe}(\text{CN})_6]^{3-/4-}$  solution. As shown in Fig. S2A,† compared with the bare SPE (curve a), the redox peak current decreased when Cu-MOFs-COOH-GO nanocomposite was modified on the electrode surface (curve b). This may be due to the weak conductivity of Cu-MOFs and the negative charges carried by COOH-GO and Nafion, which can hinder the transferring of  $[\text{Fe}(\text{CN})_6]^{3-/4-}$  probes at the electrode interface in some extent. After incubating with the MeJA antibody (curve c) and BSA (curve d) sequentially, the redox peak current of  $[\text{Fe}(\text{CN})_6]^{3-/4-}$  gradually decreased, which proved that the insulated antibody and BSA were successfully assembled on the electrode surface. When 1 nM MeJA (curve e) was added, the peak current of  $[\text{Fe}(\text{CN})_6]^{3-/4-}$  decreased further, which was caused by the steric hindrance effect of the immunocomplex produced by the specific binding of anti-MeJA and MeJA.<sup>37,38</sup>

Electrochemical impedance spectroscopy (EIS) was also used to characterize the charge transfer characteristics during the assembly process of immunosensors (Fig. S2B†). A simple equivalent circuit model (the inset in Fig. S2B†) was used to fit the impedance spectroscopy. As shown in Fig. S2B,†  $R_{\text{ct}}$  increased when Cu-MOFs-COOH-GO was modified on the electrode (curve b), compared to the smaller  $R_{\text{ct}}$  for the bare electrode (curve a). The increase of resistance may be due to the weak conductivity of Cu-MOFs and repulsive effect of the negative charge carried by COOH-GO and Nafion to  $[\text{Fe}(\text{CN})_6]^{3-/4-}$  ions. With the adding of antibody (curve c), BSA (curve d), and MeJA (curve e),  $R_{\text{ct}}$  gradually increased, due to the insulated properties of these molecules. The results of the EIS were consistent with that of CV. The CV and EIS results also confirmed the successful construction of the immunosensor for MeJA.

The effect of the scan rate  $\nu$  on the voltammetric behavior of the Cu-MOFs-COOH-GO/SPE electrode in 0.01 M PBS solution was determined. As shown in Fig. S2C,† both anodic peak current ( $I_{\text{pa}}$ ) and cathodic peak current ( $I_{\text{pc}}$ ) increased with the increase of scan rate in the range of 60–300  $\text{mV s}^{-1}$ . The  $I_{\text{pa}}$  and  $I_{\text{pc}}$  showed a linear relationship with the square root of the scan rate (the inset in Fig. S2C†), indicating that the electrode reaction on the surface of immunosensor was a diffusion-controlled surface reaction. According to the Randles-Sevcik equation, the electroactive area of Cu-MOFs-COOH-GO/SPE is 0.39  $\text{cm}^2$ . The geometric area of the bare SPE is about 0.07  $\text{cm}^2$ , so the modification of Cu-MOFs-COOH-GO nanocomposites significantly increases the effective active area of the electrode.

### 3.3. Optimization of experimental conditions

In order to improve the performance of the immunosensor, the incubation time of the antigen and antibody was optimized. The result is shown in Fig. S3A.† It is observed that the change of response current  $\Delta I$  gradually increased with the increase of the incubation time when 1 nM of MeJA was used, indicating that more and more MeJA were bound to the sensor surface. The



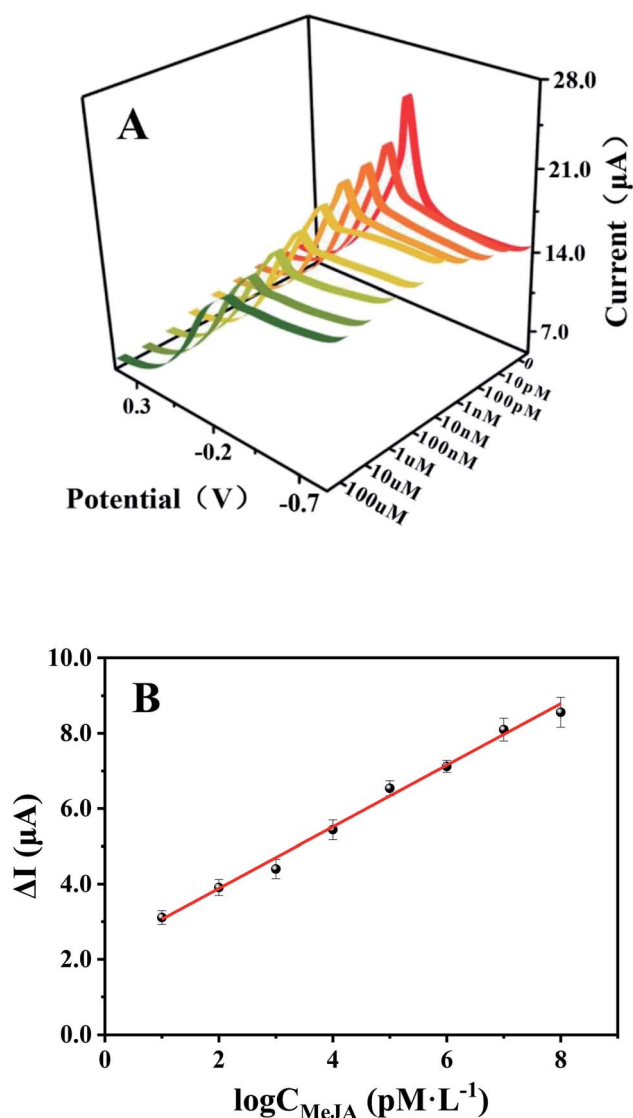


Fig. 4 (A) DPV curves of BSA/anti-MeJA/Cu-MOFs-COOH-GO/SPE in 0.01 M PBS (pH 7.4) toward different MeJA concentration. (B) The calibration curves of BSA/anti-MeJA/Cu-MOFs-COOH-GO/SPE for MeJA in the range of 10 pM to 100 μM.

maximum current response of the immunosensor was found at 60 minutes. As time goes on,  $\Delta I$  was decreased, indicating the binding between antibody and antigen has reached a saturation

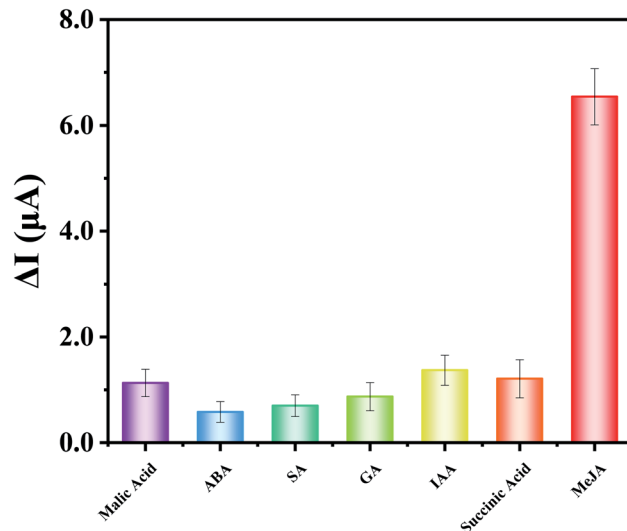


Fig. 5 The response current of BSA/anti-MeJA/Cu-MOFs-COOH-GO/SPE to different chemicals: malic acid, ABA, SA, GA, IAA, succinic acid and MeJA in 0.01 M PBS (pH 7.4). The concentrations of all the chemicals are 1 μM.

state when the incubation time is 60 minutes. Therefore, 60 min is the best choice for detecting MeJA in this work.

The effect of Cu-MOFs concentration was studied. As shown in Fig. S3B,†  $\Delta I$  gradually increased with the increase of Cu-MOFs concentration from 0.5 to 1.25 mg ml<sup>-1</sup>, and the maximum current response arrived when 1.25 mg ml<sup>-1</sup> Cu-MOFs was used. When higher concentration of Cu-MOFs was used,  $\Delta I$  did not continue to rise. Therefore, the optimal concentration of Cu-MOFs is 1.25 mg ml<sup>-1</sup>.

The COOH-GO concentration was also optimized. Fig. S3C† shows the effect of COOH-GO concentration on the change of response current  $\Delta I$ . Due to the excellent electron transfer ability of COOH-GO,  $\Delta I$  gradually increased when the COOH-GO contents were from 0.5 mg ml<sup>-1</sup> to 1.0 mg ml<sup>-1</sup>.  $\Delta I$  gradually decreased when 1.0 to 2.5 mg ml<sup>-1</sup> COOH-GO were used. Thus, 1.0 mg ml<sup>-1</sup> of COOH-GO is the optimal in this study.

It is necessary and effective to optimize the antibody concentration immobilized on the electrode surface to improve the sensitivity of immunosensor. As shown in Fig. S3D,†  $\Delta I$  gradually increased with the antibody concentration from 0.01 to 0.15 mg ml<sup>-1</sup>, but it decreased when the antibody

Table 1 Comparisons of the as-prepared MeJA sensor with the previous reported MeJA detection methods

Electrode	Method	Linear range (mol L <sup>-1</sup> )	LOD (mol L <sup>-1</sup> )	Ref.
—	ELISA	$4.46 \times 10^{-10}$ – $4.46 \times 10^{-7}$	$8.92 \times 10^{-10}$	39
—	GC-MS	$4.46 \times 10^{-9}$ – $4.46 \times 10^{-7}$	$1.15 \times 10^{-9}$	40
—	HPLC	$2.23 \times 10^{-8}$ – $8.92 \times 10^{-6}$	$4.46 \times 10^{-9}$	41
—	LC-MS-MS	$8.92 \times 10^{-10}$ – $4.46 \times 10^{-6}$	$3.34 \times 10^{-10}$	42
Nano-MMT/GCE	First-SWV	$7.00 \times 10^{-7}$ – $1.00 \times 10^{-3}$	$5.00 \times 10^{-7}$	43
PTA/NR-MMT/GE	DPV	$5.00 \times 10^{-7}$ – $8.00 \times 10^{-5}$	$2.00 \times 10^{-7}$	44
PTA/GO	DPV	$5.00 \times 10^{-7}$ – $8.00 \times 10^{-5}$	$2.00 \times 10^{-7}$	45
rGO-PST/GCE	First-LSV	$1.00 \times 10^{-6}$ – $1.00 \times 10^{-5}$ , $3.00 \times 10^{-5}$ – $3.00 \times 10^{-3}$	$5.00 \times 10^{-7}$	46
BSA/Ab/Cu-MOFs-COOH-GO/SPE	DPV	$1.00 \times 10^{-11}$ – $1.00 \times 10^{-4}$	$3.50 \times 10^{-13}$	This work

Table 2 Recovery of MeJA in grape fruit samples ( $n = 5$ )

Initial concentration (nM)	Added levels (nM)	Method	Recovery/%					<i>t</i>
$9.92 \pm 1.66$ (sensor)	4.5	Sensor	103.5	99.2	110.8	101.0	91.6	0.26
		ELISA	95.3	105.2	92.5	107.6	89.9	
$9.37 \pm 1.51$ (ELISA)	45	Sensor	95.5	106.8	93.7	105.7	89.7	0.39
		ELISA	107.4	93.6	98.9	95.4	102.2	
	360	Sensor	95.8	89.8	103.3	91.6	98.1	0.49
		ELISA	106.0	94.2	89.7	97.1	91.3	

concentration continued to increase to  $0.20 \text{ mg ml}^{-1}$ . This is mainly due to the comprehensive effect of the immobilization capacity of Cu-MOF-COOH-GO nanocomposite for antibody on the sensor surface and spatial hindrance of the immune response. Hence, the optimal concentration of the antibody is  $0.15 \text{ mg ml}^{-1}$  in this study.

### 3.4. Performance of the Cu-MOFs-COOH-GO immunosensor for detecting MeJA

DPV was used to conduct quantitative analysis of MeJA by the fabricated immunosensors. Under the optimal experimental conditions, the immunosensor was incubated with different concentrations of MeJA ( $0\text{--}100 \text{ }\mu\text{M}$ ) at room temperature for 1 hour. The DPV response curves in PBS ( $0.01 \text{ M}$  pH 7.4) are shown in Fig. 4A. It is clearly observed that with the increased concentrations of MeJA, the oxidation peak current of the sensor gradually decreased. This is mainly due to the insulating nature of the antibody-antigen complex formed by Anti-MeJA and MeJA, which hinders the electron transfer of Cu-MOFs on the electrode surface. Therefore, the current change is positively correlated with the corresponding MeJA concentration. The change of the response current ( $\Delta I$ ) and the logarithmic value of MeJA concentration shows a linear relationship over a wide range from  $10 \text{ pM}$  to  $100 \text{ }\mu\text{M}$  (Fig. 4B). The linear regression equation is  $\Delta I (\mu\text{A}) = 0.8179 \log C_{\text{MeJA}} (\text{pM L}^{-1}) + 2.2461$ , and the correlation coefficient is 0.9938. The limit of detection (LOD) of MeJA is  $0.35 \text{ pM}$  ( $S/N = 3$ ). Compared with various MeJA detection methods which reported in the previous literature<sup>39–46</sup> (Table 1), the as-prepared immunosensor has the lowest LOD and the widest detection range so far, and its range can cover the whole concentration range of MeJA in most plants, which is in the range of  $0.01 \text{ ng g}^{-1}$  to  $1500 \text{ ng g}^{-1}$ .<sup>47,48</sup> The excellent performance of the sensor is mainly due to two reasons, one is that the film formed by nanocomposites increases the effective active area of the electrode, and the application of COOH-GO also increases the amount of immobilized antibody. Second, the combination of COOH-GO with Cu-MOF enhances the oxidation signal of Cu-MOFs due to their synergistic effect, thus increasing the detection capacity of the sensor.

To analyze the selectivity of immunosensor, several potential interferences were tested, including malic acid, abscisic acid, salicylic acid, gibberellin, indole-3-acetic, and succinic acid. As shown in Fig. 5, the change of the response current ( $\Delta I$ ) of MeJA ( $100 \text{ nM}$ ) is much higher than other potential interferences under the concentration of  $1 \text{ }\mu\text{M}$ , indicating that the developed

immunosensor has acceptable selectivity for MeJA due to the specific binding ability of monoclonal antibody to antigen. The RSD is 7.6% for 5 different BSA/anti-MeJA/Cu-MOFs-COOH-GO/SPE immunosensors in presence of  $1 \text{ nM}$  MeJA. After storing at  $4 \text{ }^\circ\text{C}$  for two weeks, the immunosensor still maintains 93.3% of the initial response current, which indicated that the sensor is highly stable.

### 3.5. Real sample analysis

In order to investigate the practical applications of the as-prepared immunosensor, standard addition method was employed to detect MeJA in grape fruit samples. The initial concentration of MeJA in 100% grape fruit samples was detected by our sensor. This result was compared with that of a commercial ELISA kits for MeJA (obtained from China Agricultural University). The relative error is from  $-1.22$  to  $11.81\%$  (Table S1†), which indicates that the two methods are in acceptable agreement. After dilution, different amounts of MeJA were added to grape fruit samples. The equivalence of the two detection methods was also evaluated by *t*-test. Significance level  $\alpha$  (0.05) was selected. As shown in Table 2, there was no significant difference between the two methods and the present immunosensor might provide an effective tool for determining MeJA.

## 4. Conclusions

In summary, an electrochemical immunosensor for MeJA based on Cu-MOFs-COOH-GO platform was developed in this work. The good synergistic effect of Cu-MOFs and COOH-GO makes the immunosensor has the advantages of wide linear range, and low detection limit. This platform is simple, low cost, and does not need redox probe solutions for measurements. It shows a remarkable potential for on-site application in precision agriculture.

## Conflicts of interest

There are no conflicts to declare.

## Acknowledgements

The authors are thankful for the fundings from the National Natural Science Foundation of China (Grant no. 21974012), Beijing Natural Science Foundation (2222007), and Key-Area



Research and Development Program of Guang Dong Province (No. 2019B020219002).

## References

- 1 Z. Peng and Y. Zhang, *Mol. Med. Rep.*, 2017, **15**, 957–962.
- 2 S. M. Gunjegaonkar and T. S. Shanmugarajan, *Plant Signaling Behav.*, 2019, **14**, e1642038.
- 3 A. Hanaka and R. Nurzyńska-Wierdak, *Acta Sci. Pol. Hortorum Cultus*, 2019, **18**, 237–249.
- 4 M. Asghari and A. R. Hasanlooe, *Food Sci. Nutr.*, 2016, **4**, 377–383.
- 5 J. Li, K. Chen, F. Wang, W. Dai, S. Li, J. Feng, L. Wu, T. Liu, S. Xu, Y. Xia, J. Lu, Y. Zhou, L. Xu and C. Guo, *Oncotarget*, 2017, **8**, 45965–45980.
- 6 H. Li, Y. Hu, A. Li, X. Wang, P. Hou, C. Wang, K. Chen and C. Zhao, *RSC Adv.*, 2017, **7**, 54416–54421.
- 7 Z. Su, X. Xu, Y. Cheng, Y. Tan, L. Xiao, D. Tang, H. Jiang, X. Qin and H. Wang, *Nanoscale*, 2019, **11**, 962–967.
- 8 R. Wang, Y. Li, Q. Li, G. Shen and L. Xiao, *Anal. Lett.*, 2009, **42**, 2893–2904.
- 9 J. Li, L. Xiao, G. Zeng, G. Huang, G. Shen and R. Yu, *J. Agric. Food Chem.*, 2005, **53**, 1348–1353.
- 10 H. Wang, X. Gao and Z. Ma, *Sci. Rep.*, 2017, **7**, 1023.
- 11 T. Z. Liu, R. Hu, X. Zhang, K. L. Zhang, Y. Liu, X. B. Zhang, R. Y. Bai, D. Li and Y. H. Yang, *Anal. Chem.*, 2016, **88**, 12516–12523.
- 12 F. T. C. Moreira, B. A. G. Rodriguez, R. A. F. Dutra and M. G. F. Sales, *Sens. Actuators, B*, 2018, **264**, 1–9.
- 13 E. K. G. Trindade and R. F. Dutra, *Colloids Surf., B*, 2018, **172**, 272–279.
- 14 K. Yamanaka, M. C. Vestergaard and E. Tamiya, *Sensors*, 2016, **16**, 1761.
- 15 G. Xing, B. Luo, J. Qin, X. Wang, P. Hou, H. Zhang, C. Wang, J. Wang and A. Li, *Talanta*, 2021, **232**, 122477.
- 16 C. Duan and J. Zheng, *J. Electrochem. Soc.*, 2019, **166**, B942–B947.
- 17 S. Dong, G. Suo, N. Li, Z. Chen, L. Peng, Y. Fu, Q. Yang and T. Huang, *Sens. Actuators, B*, 2016, **222**, 972–979.
- 18 Y. Song, M. Xu, C. Gong, Y. Shen, L. Wang, Y. Xie and L. Wang, *Sens. Actuators, B*, 2018, **257**, 792–799.
- 19 X. Fang, B. Zong and S. Mao, *Nanomicro Lett.*, 2018, **10**, 64.
- 20 Y. Zhang, A. Nsabimana, L. Zhu, X. Bo, C. Han, M. Li and L. Guo, *Talanta*, 2014, **129**, 55–62.
- 21 S. Rani, S. Kapoor, B. Sharma, S. Kumar, R. Malhotra and N. Dilbaghi, *J. Alloys Compd.*, 2020, **816**, 152509.
- 22 T. Wu, T. Li, Z. Liu, Y. Guo and C. Dong, *Talanta*, 2017, **164**, 556–562.
- 23 A. Yiğit, Y. Yardım, M. Çelebi, A. Levent and Z. Şentürk, *Talanta*, 2016, **158**, 21–29.
- 24 W. J. Shen, Y. Zhuo, Y. Q. Chai and R. Yuan, *Anal. Chem.*, 2015, **87**, 11345–11352.
- 25 J. Li, D. Liu, B. Li, J. Wang, S. Han, L. Liu and H. Wei, *CrystEngComm*, 2015, **17**, 520–525.
- 26 M. S. Seehraa, V. Narang, U. K. Geddam and A. B. Stefaniak, *Carbon*, 2017, **111**, 380–384.
- 27 S. Rostamnia, H. Alamgholiloo and X. Liu, *J. Colloid Interface Sci.*, 2016, **469**, 310–317.
- 28 C. G. Carson, K. Hardcastle, J. Schwartz, X. Liu, C. Hoffmann, R. A. Gerhardt and R. Tannenbaum, *Eur. J. Inorg. Chem.*, 2009, 2338–2343.
- 29 X. Zhao, S. Liu, Z. Tang, H. Niu, Y. Cai, W. Meng, F. Wu and J. P. Giesy, *Sci. Rep.*, 2015, **5**, 11849–11854.
- 30 W. Siew, N. A. Bakar and M. A. Bakar, *Inorg. Chim. Acta*, 2018, **482**, 53–61.
- 31 M. D. Firouzjaei, F. A. Afkhami, M. R. Esfahani, C. H. Turner and S. Nejati, *J. Water Proc. Eng.*, 2020, **34**, 101180.
- 32 S. Singh, A. Numan, Y. Zhan, V. Singh, T. Van Hung and N. D. Nam, *J. Hazard. Mater.*, 2020, **399**, 123042.
- 33 Q.-Q. Xu, B. Liu, L. Xu and H. Jiao, *J. Solid State Chem.*, 2017, **247**, 1–7.
- 34 A. R. Abbasi, M. Karimi and K. Daasbjerg, *Ultrason. Sonochem.*, 2017, **37**, 182–191.
- 35 Y. Feng, H. Jiang, S. Li, J. Wang, X. Jing, Y. Wang and M. Chen, *Colloids Surf., A*, 2013, **431**, 87–92.
- 36 H. Saedi, M. R. Fat'hi and B. Zargar, *J. Chin. Chem. Soc.*, 2021, 1–11.
- 37 J. Liu, J. Wang, T. Wang, D. Li, F. Xi, J. Wang and E. Wang, *Biosens. Bioelectron.*, 2015, **65**, 281–286.
- 38 C. Thunkhamrak, P. Chuntib, K. Ounnunkad, P. Banet, P. H. Aubert, G. Saianand, A. I. Gopalan and J. Jakmunee, *Talanta*, 2020, **208**, 120389.
- 39 M. Yi, L. Zhao, K. Wu, C. Liu, D. Deng, K. Zhao, J. Li and A. Deng, *Analyst*, 2020, **145**, 4004–4011.
- 40 W. Ma, S. Fu, Y. Hashi and Z. Chen, *J. Agric. Food Chem.*, 2013, **61**, 6288–6292.
- 41 X. Yu, X. Ling, L. Zou and Z. Chen, *J. Sep. Sci.*, 2017, **40**, 1556–1563.
- 42 X. Liu, Y. Yang, W. Lin, J. Tong, Z. Huang and L. Xiao, *Chin. Sci. Bull.*, 2010, **55**, 2231–2235.
- 43 T. Gan, C. Hu, Z. Chen and S. Hu, *J. Agric. Food Chem.*, 2010, **58**, 8942–8947.
- 44 T. Gan, C. Hu, Z. Chen and S. Hu, *Electrochim. Acta*, 2011, **56**, 4512–4517.
- 45 T. Gan, C. Hu, Z. Chen and S. Hu, *Sens. Actuators, B*, 2010, **151**, 8–14.
- 46 J. Sun, Z. Wu, D. Hu, Z. Shi and Z. Lv, *Fullerenes, Nanotubes, Carbon Nanostruct.*, 2014, **23**, 701–708.
- 47 S. M. Wilbert, L. H. Ericsson and M. P. Gordon, *Anal. Biochem.*, 1998, **257**, 186–194.
- 48 P. Ahmad, S. Rasool, A. Gul, S. A. Sheikh, N. A. Akram, M. Ashraf, A. M. Kazi and S. Gucel, *Front. Plant Sci.*, 2016, **7**, 813.

